ELSEVIER

Thermochimica Acta 276 (1996) 243–256

thermochimica acta

Binary phase diagram of molecular alloys of the consecutive even-numbered *n*-alkanes *n*-tetracosane (*n*-$C_{24}H_{50}$) and *n*-hexacosane (*n*-$C_{26}H_{54}$)

Z. Achour-Boudjema, M. Bouroukba, M. Dirand*

Laboratoire de Thermodynamique Chimique et Appliquée, Ecole Nationale Supérieure des Industries Chimiques, Institut National Polytechnique de Lorraine, 1, ue Grandville. BP 451. F54001 Nancy Cédex, France

Received 27 March 1995; accepted 10 September 1995

Abstract

The phase diagram of molecular alloys of *n*-tetracosane (*n*-$C_{24}H_{50}$) and *n*-hexacosane (*n*-$C_{26}H_{54}$) has been established by a joint thermodynamic and structural study of twenty five compositions. At "low temperatures" it shows the existence of two limited domains of terminal solid solutions $\gamma_0(C_{24})$ and $\gamma_0(C_{26})$ and of three orthorhombic intermediate phases, denoted β'_1, β'' and β'_2. With increasing temperatures, these five solid solutions undergo the same solid–solid transitions as those observed in the even-numbered and odd-numbered pure *n*-alkanes and in the system *n*-docosane (*n*-$C_{22}H_{46}$)–*n*-tetracosane (*n*-$C_{24}H_{50}$), i.e.:

$\gamma_0(C_{24})$ and $\gamma_0(C_{26})$ → Rotator phase α-RII ($R\bar{3}m$) → Liquid

β'_1, β'_2 and β'' → Rotator phase β-RI (Fmmm) → α-RII → Liquid

Keywords: Binary phase diagram; Differential enthalpimetry; DTA; DSC; Molecular alloy *n*-Hexacosane; Molecular alloy *n*-Tetracosane; X-ray diffraction

1. Introduction

Study of the structural evolution of mixtures of the two *n*-alkanes *n*-tetracosane (*n*-$C_{24}H_{50}$) and *n*-hexacosane (*n*-$C_{26}H_{54}$) of varying concentration at 293 K [1] has

* Corresponding author. Tel.: +33 83 17 50 00; Fax: +33 83 35 08 11; e-mail: dirand@ensic.u-nancy.fr; http://www.ensic.u-nancy.fr/

0040-6031/96/$15.00 © 1996 – Elsevier Science B.V. All rights reserved
SSDI 0040-6031(95)02734-3

enabled us to demonstrate the existence of (for simplicity, *n*-docosane (n-$C_{22}H_{46}$), *n*-tetracosane (n-$C_{24}H_{50}$) and *n*-hexacosane (n-$C_{26}H_{54}$) respectively, are denoted, C_{22}, C_{24} and C_{26}):

(1) two terminal solid solutions, denoted $\gamma_0(C_{24})$ and $\gamma_0(C_{26})$, which have the structure of pure *n*-alkanes; and

(2) three orthorhombic intermediate phases denoted β'_1, β'_2 and β'' isomorphous with the odd-numbered *n*-alkane structure. They are isostructural with the three intermediate solid solutions which have been observed in the system C_{22}–C_{24}, also denoted β'_1, β'_2 and β'' [2–4]. The structure of one of these phases has been determined by Gerson and Nyburg [5]. On the basis of powder X-ray diffraction photographs, the phases β'_1 and β'_2 are indistinguishable.

Despite what is generally found in the literature for binary systems with two consecutive even-numbered *n*-alkanes [6–9], these results show that these binary mixtures do not form an orthorhombic continuous homogeneous solid solution at "low temperature" even if the two pure components are triclinic or monoclinic: this is not compatible with Palatnik and Landau's rule [10] on adjacent phase domains.

With increasing temperature, as for the system C_{22}–C_{24} [2–4]:

(1) the $\gamma_0(C_{24})$ and $\gamma_0(C_{26})$ terminal solid solutions undergo solid–solid transitions identical with those of the even-numbered *n*-alkanes (C_{24} and C_{26}) [11–13]; and

(2) the three orthorhombic intermediate solid solutions β'_1, β'' and β'_2 present the same solid–solid transitions as those observed in the odd-numbered pure *n*-alkanes, *n*-tricosane or *n*-pentacosane [1, 14–20].

Our purpose is to establish the phase diagram of C_{24}–C_{26} mixtures and to show its similarity with that of the system C_{22}–C_{24} [3]. The study of structural and thermodynamic behaviour when varying the molar concentration and temperature has been realized by differential thermal analysis, differential enthalpimetry, and X-ray diffraction of twenty five samples.

2. Experimental

2.1. Samples

The C_{24} and C_{26} *n*-alkanes were purchased from Aldrich chemical company; their purity, as determined by gas chromatography and mass spectrometry, was 99 mole percent.

The samples were prepared by weighing together the solid components, melting and thorough mixing. The homogeneous liquid solution thus obtained was quenched in a crystallizing dish maintained at a very low temperature in a Dewar vessel filled with liquid air. Such rapid cooling ensured a uniform steric concentration of each component in the solid. Table 1 shows the masses of C_{24} and C_{26} and the corresponding mole fractions of each analysed sample.

Table 1
Molar compositions of C_{26} and corresponding masses of C_{24} and C_{26} for the mixtures studied

Molar composition in mol% of C_{26}	Mass of *n*-tetracosane in mg[a]	Mass of *n*-hexacosane in mg[b]
1.1	1.9764	0.0236
2.5	1.9580	0.0538
5.1	2.8341	0.1659
10	2.6778	0.3222
15.1	2.5171	0.4829
20	2.3599	0.6401
25	2.2043	0.7957
30.1	1.8923	0.9537
33	1.3042	0.6957
35.2	1.2587	0.7413
40.1	1.5871	1.2608
45.1	1.4475	1.4129
45.9	1.0426	0.9574
49.8	1.2621	1.5525
56	1.1408	1.7379
60.1	0.7605	1.2395
64.6	1.0069	1.9931
75	0.4704	1.5296
77.1	0.4305	1.5695
80	0.5619	2.4381
85	0.4207	2.5793
90.1	0.2778	2.7222
95	0.1407	2.8593
97	0.0554	1.9446
99	0.0369	1.9631

[a] Molecular mass 338.6590 g mol^{-1}
[b] Molecular mass 366.7126 g mol^{-1}

2.2. *X-ray diffraction*

X-ray diffraction experiments were carried out on powder samples using $\lambda_{K\alpha}$ copper radiation. The X-ray patterns were obtained with a CGR diffractometer using a focussed monochromatic beam, obtained with a filament intensity of 10 mA at 48 kV.

The line positions were measured with an accuracy of 0.05° for the values determined by the CGR diffractometer. Calibration was performed using pure aluminium standards. The X-ray diffractometer analyses were performed at different temperatures with the help of a heated sample holder. The heating of the sample holder was based on the Peltier effect; the precision of the sample temperature was within $\pm$ 0.2°C of the set point.

2.3. *Differential scanning calorimetry*

2.3.1. *Device-Principle of measurement*

The measurements were performed with a differential scanning DSC 111 Setaram calorimeter of the Tian Calvet type [21]. The temperature was programmed in continuous or discontinuous modes.

This calorimeter is based on the Calvet principle which uses differential detection of the thermal flow between the measuring and the reference cells and the thermoregulated block. The apparatus is composed of two thermoelectric piles surrounding the calorimetric cells and connected together in opposition (differential arrangement). Each pile consists of a regular distribution of thermocouples around the cell. The electromotive force (e.m.f.) developed in them is directly proportional to the flow of heat from the cell (Fig. 1). The e.m.f. measured from time t_1 to time t_2 is related to the heat difference, Q_T, exchanged between the cells and the calorimeter wall by means of the coefficient of sensitivity of the apparatus, denoted S:

$$Q_T = \frac{1}{S}\int_{t_1}^{t_2} \Delta E \, dt$$

The calibration of the calorimeter was performed with alumina of the "National Bureau of Standards"; its thermodynamic properties are perfectly well known [22]. This measurement enables us to determine the coefficient S.

2.3.2. Differential thermal analysis (continuous mode)

The calorimetric measurements were made with linear and continuous programming of the temperature with a computer, which also collected and stored the measured heat-flow data. The samples were alternately heated and cooled at a rate of 0.5° min^{-1} to separate the different peaks which appeared, and the transition temperatures were detected.

2.3.3. Differential enthalpimetry (discontinuous mode)

The calorimetric measurements were carried out with discontinuous programming of the temperature with time. These measurements enabled us to determine the values of the enthalpy variation when varying the temperatures for each sample.

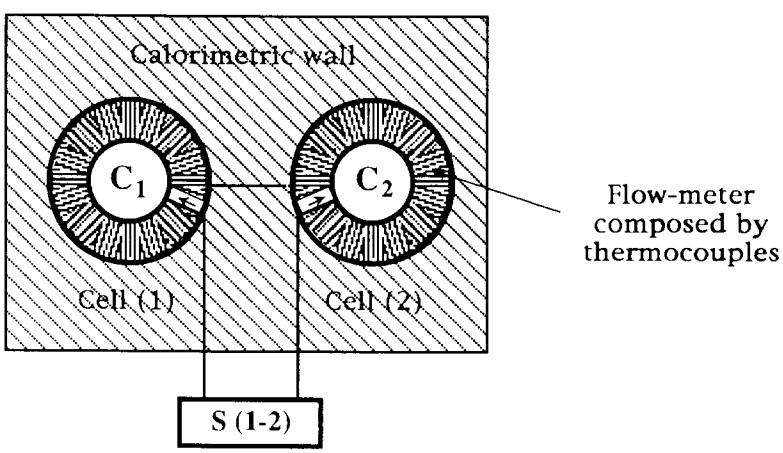

Fig. 1. Measurement of the differential signal.

The calorimeter temperature is programmed as shown in Fig. 2; it increases linearly between T_1 and T_2 and is then kept constant at T_2 for a time t_p. The calorimeter temperature increases step by step, from the first temperature to the maximum temperature of the experiment. The difference $(T_2 - T_1)$ is always 0.5 K, and the rise time (t_m) is set at 180 s; the time t_p depends on an automatic test made by computer, checking that the calorimetric signal has returned to a constant value, corresponding to a steady state (Fig. 2).

For each temperature jump from T_1 to T_2, the amount of heat Q_T exchanged between the cells and the calorimeter wall is directly related to the enthalpy variation between T_1 and T_2:

$$\Delta H_{T_1}^{T_2} = H_{T_2}^0 - H_{T_1}^0 = \frac{M}{m} Q_T$$

M and m are, respectively, the molecular weight and the mass of the sample placed in (or introduced into) the calorimeter.

The temperatures of transformation were obtained from the curves of enthalpy variation as a function of temperature.

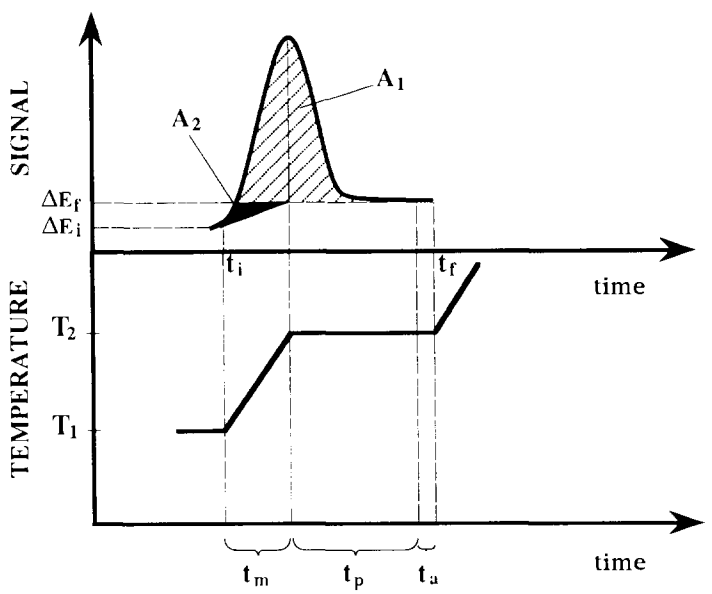

Fig. 2. Typical programmed temperature and calorimetric signal when the temperature increases from T_1 to T_2 in the discontinuous mode.

2.3.4. Calibration

Calibration of the temperatures was performed with gallium and indium as standards in the continuous mode and with gallium, indium and dibenzoyl in the discontinuous mode (Table 2). The calorimetric measurements were made on C_{24} and C_{26} and on twenty five binary mixtures covering the whole range of molar composition.

3. Results

3.1. Procedure

The peaks which appear during DTA analysis enable determination of the temperature ranges of the solid–solid and solid–liquid transitions (Fig. 3). The X-ray diffraction analysis defines their structural evolution with temperature (± 0.2°C) (Fig. 4). The differential enthalpimetric analysis (Fig. 5) confirms the values of these transition and melting temperatures, which were determined with an accuracy of ± 0.25°C.

3.2. Structural evolution

On the basis of powder X-ray diffraction experiments [1]:

(1) the terminal solid solutions $\gamma_0(C_{22})$, $\gamma_0(C_{24})$ and $\gamma_0(C_{26})$ are indistinguishable, except for the long *c* axis variation;

(2) the orthorhombic intermediate phases β'_1, β'' and β'_2 of the C_{24}–C_{26} system are isostructural with the orthorhombic phases β'_1, β'' and β'_2, respectively, of the C_{22}–C_{24} system; and

(3) the structural behaviour of the C_{24}–C_{26} mixtures with increasing temperature is identical with that observed in the C_{22}–C_{24} and C_{23}–C_{24} systems [1,3,4,20,23] (Fig. 4).

Thus, when molar concentrations and temperatures are varied, the X-ray patterns of C_{24}–C_{26} mixtures evolve in the same way as those described previously for the C_{22}–C_{24} system [1,3,4,20]:

Table 2
Calibration of the temperatures using gallium and indium for continuous temperature programming and gallium, indium and dibenzoyl in discontinuous mode

	Temperatures of melting in the continuous mode in K		Temperatures of melting in the discontinuous mode in K	
	Experimental	Literature	Experimental	Literature
Gallium	303.1	303	302.4	303
Indium	430.7	429.8	429.2	429.8
Dibenzoyl	–	–	368	368.2

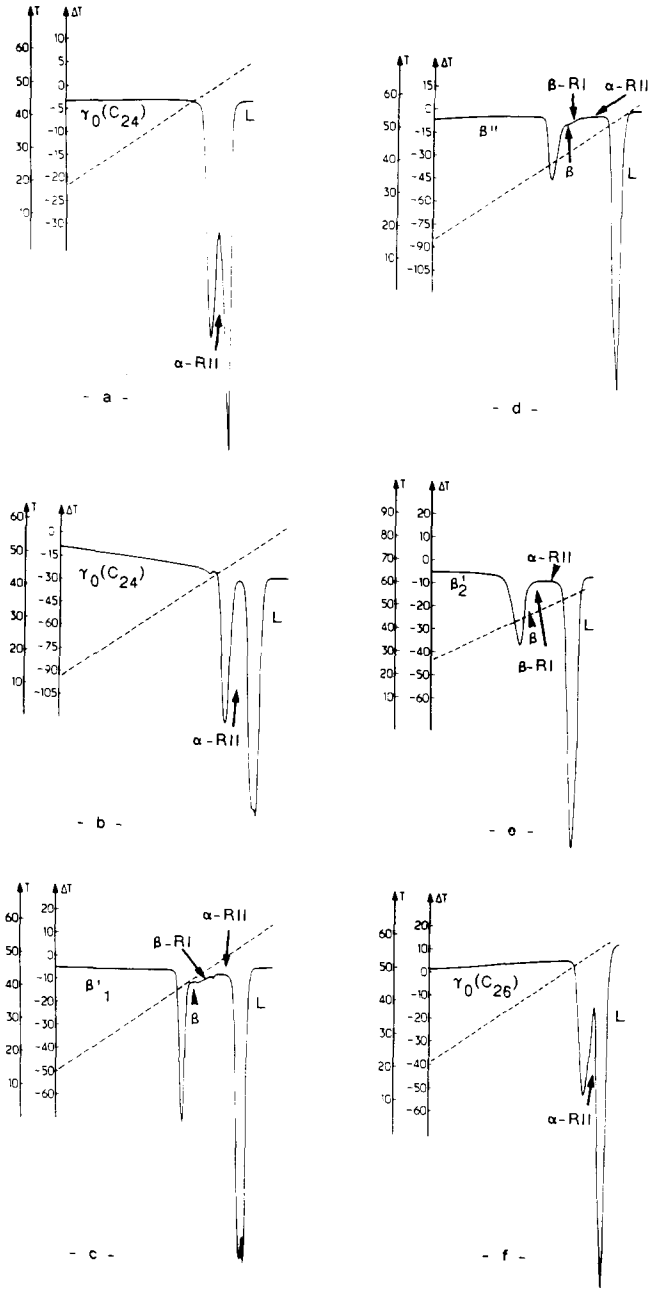

Fig. 3. DTA curves for several C_{24}–C_{26} binary mixtures of different molar composition: (a) 100% C_{24}, (b) 1.1% C_{26}, (c) 10% C_{26}, (d) 40.1% C_{26}, (e) 75% C_{26}, (f) 100% C_{26}.

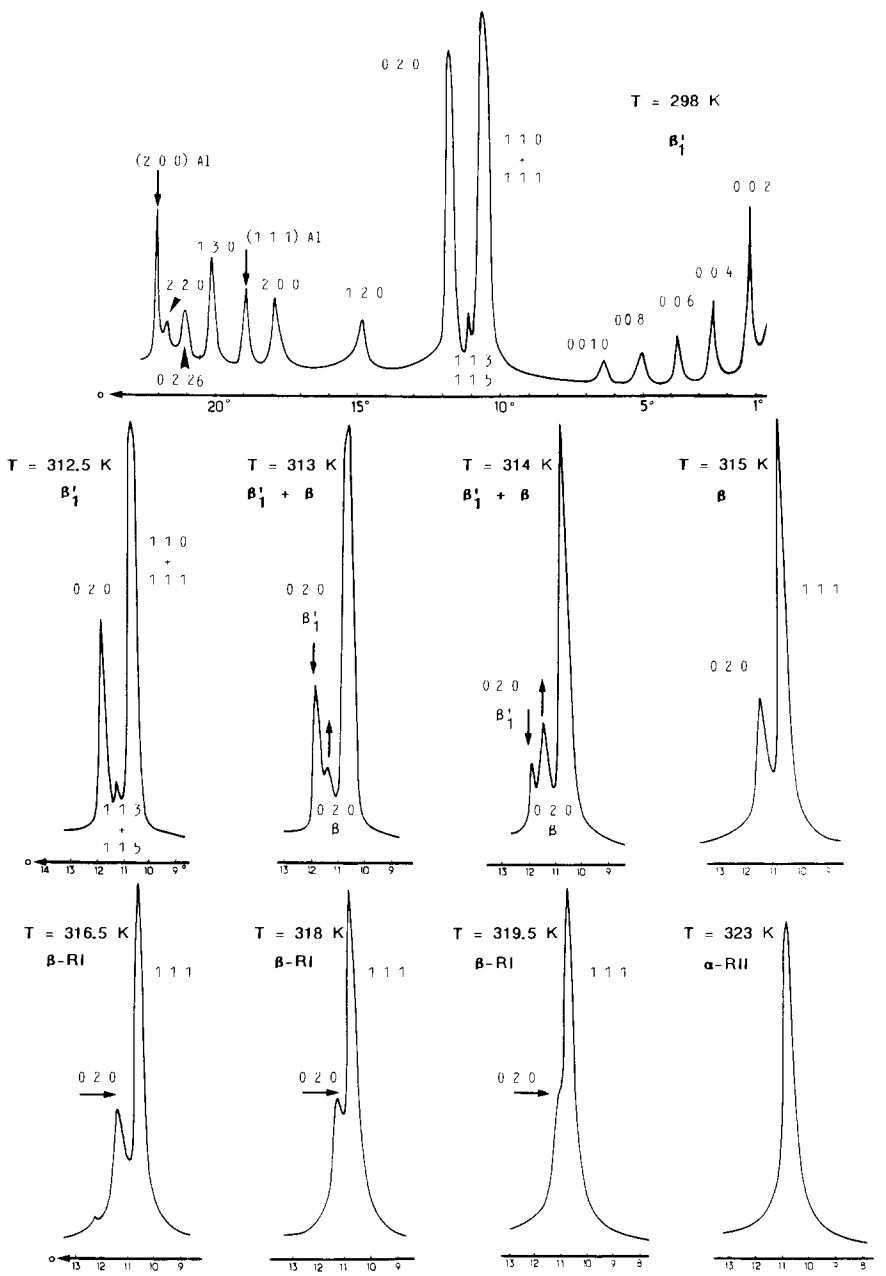

Fig. 4. X-ray diffractogram of evolution of the phase β'_1 (10 mol% C_{26}) with increasing temperature.

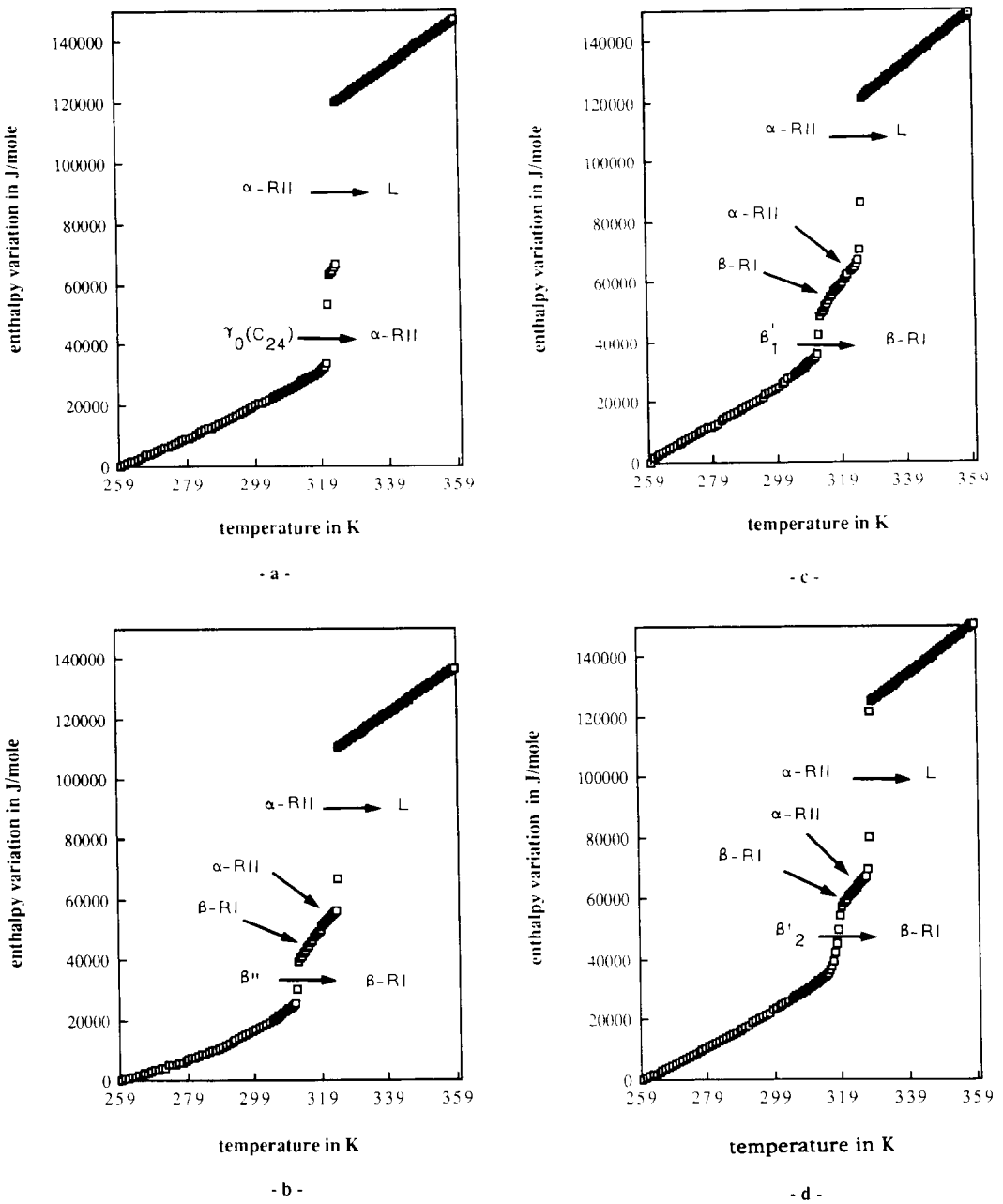

Fig. 5. Curves corresponding to the enthalpy variation, with increasing temperature, for several C_{24}–C_{26} mixtures of different composition: (a) 100% C_{24}, (b) 15.1% C_{26}, (c) 35.2% C_{26}, (d) 80% C_{26}.

(1) in single-phase domains, only lattice parameters vary; and

(2) in two-phase regions, the relative intensities of characteristic diffraction lines of each phase (appearance, disappearance or variation) change; the crystalline parameters of each solid solution are constant.

Fig. 4 illustrates the evolution of the X-ray diffraction pattern of phase β'_1 (10 mol% C_{26}) with increasing temperature. The phases β'_2 and β'' [1] present the same behaviour when the temperature increases. These results show that the orthorhombic intermediate phases β'_1, β'_2 and β'' undergo the same solid–solid transitions as the odd-numbered pure *n*-alkanes (C_{23} and C_{25}) [1,15,17] above their transition δ up to their melting point as was described, also for the systems C_{22}–C_{24} and C_{23}–C_{24} [3,23].

The solid phase succession from "low" to "high temperatures" for the phases β'_1, β'_2 or β'' corresponds to the following diagram.

← Low Temperatures | High Temperatures →

β'_1, β'_2 or β'' →|← β–RI →|← α-RII →|← liquid

|← crystal phases →|← "plastic" or Rotator phases →|

|← orthorhombic structure →|← rhombohedral structure →|

|← intermediate phases →|← Fmmm →|← $R\bar{3}m$ →|

(1) The occurrence of the phase β (Fmmm) is accompanied by considerable increases in the unit cell base area (*a*, *b*), [3,17,20]; an important shift of the line (020) is observed (Fig. 4).

(2) The diffraction peak (020) then moves progressively to the diffraction line (111); the *b*/*a* parameter ratio increases progressively with temperature (Fig. 4). This structural evolution characterizes the Rotator state β-RI (Fmmm).

(3) When the two peaks (020) and (111) coincide, the sub-cell is hexagonal ($b/a = \sqrt{3}$), which corresponds to the appearance of the rhombohedral Rotator phase α-RII ($R\bar{3}m$): the stacking mode along the long c axis of the chains is ABCABC [17] instead of ABAB in the Rotator phase β-RI (Fmmm) [17,19]. The space groups Fmmm of the orthorhombic Rotator phase β-RI and $R\bar{3}m$ of the Rotator phase α-RII have been respectively determined by Ungar [17], and Ungar and Masic [19].

3.3. *Differential thermal analysis*

Figs. 3 and 5 illustrate, respectively, typical DTA curves and enthalpimetric curves from this system. On the DTA curves (Fig. 3) as the temperature is increased the first peak corresponds to the solid–solid transition (β'_1, β'_2 or $\beta'' \rightarrow \beta$) which is accompanied by an important enthalpy effect (Fig. 5). The region near the β-RI state is characterized by a differential signal which does not return to the baseline over a wide temperature range, with abnormal enthalpy consumption (Figs. 3 and 5); this evolution of structural and thermodynamic properties is probably a transition of a second or higher order [17,19]. Next, the small peak corresponds to the first order solid–solid transition β-RI (Fmmm) → α-RII ($R\bar{3}m$). The last peak characterizes the α-RII–liquid equilibria.

Figs. 6 and 7 show the C_{24}–C_{26} phase diagram with two possibilities for the evolution of the phase β'' with increasing temperature: a peritectoid decomposition $\beta'' \rightarrow \beta'_2 + \beta$-RI; a solid–solid transition $\beta'' \rightarrow \beta$-RI crossing the two-phase domain ($\beta'' + \beta$-RI).

3.4. Remark concerning the C_{20}–C_{22} phase diagram

These results (Figs. 6 and 7) show the similarity between the C_{20}–C_{22} phase diagram, published by Luth and Nyburg [24] and both the C_{22}–C_{24} [3] and C_{24}–C_{26} systems, except for the "high temperature" region below the solidus line of C_{20}–C_{22} mixtures.

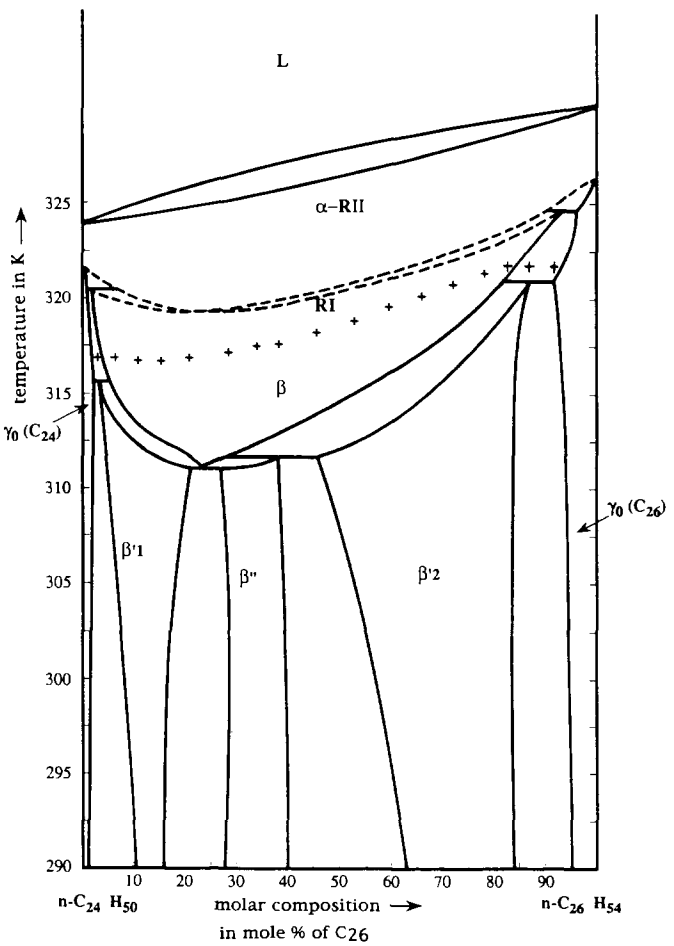

Fig. 6. Experimental phase diagram of the C_{24}–C_{26} binary system with a peritectoid decomposition: $\beta'' \rightarrow \beta'_2 + \beta$-RI. + + + + beginning temperature of Rotator state (β-RI) phenomenon.

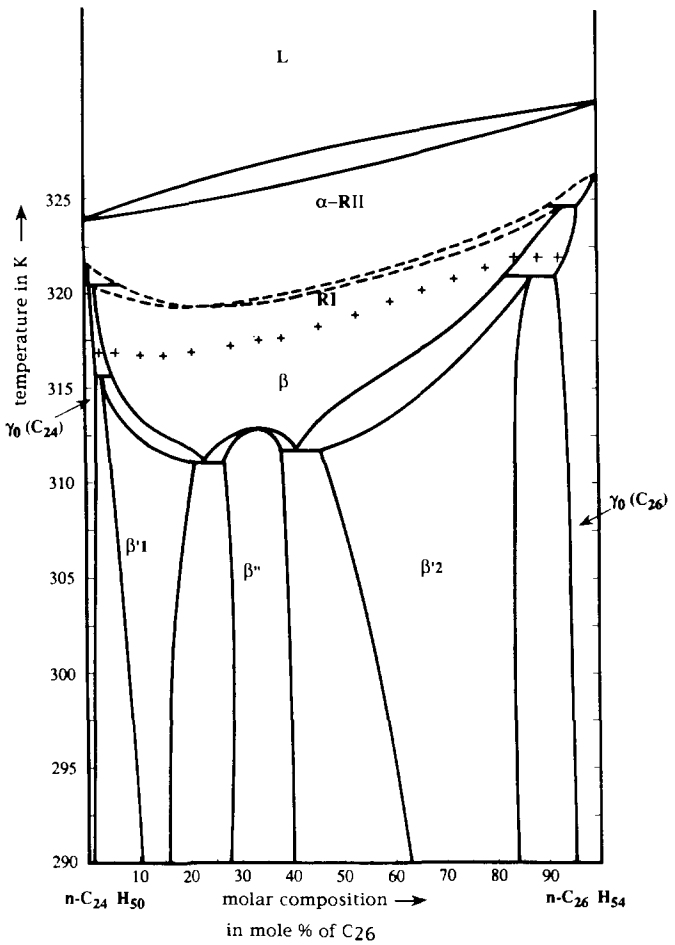

Fig. 7. Experimental phase diagram of the C_{24}–C_{26} binary system with a solid–solid transition: $\beta'' \rightarrow \beta$-RI crossing the two-phase domain ($\beta'' + \beta$-RI). + + + + beginning temperature of Rotator state (β-RI) phenomenon.

According to the C_{20}–C_{22} phase diagram of Luth and Nyburg [23]:

(1) the two pure even-numbered *n*-alkanes (C_{20} and C_{22}) undergo a γ_0 (C_{20} and C_{22})→rhombohedral phase α-RII ($R\bar{3}m$) solid–solid transition below the melting point [11–14],

(2) a continuous solid solution with an orthorhombic structure (Fmmm) [4] denoted β_0 by Luth and Nyburg [24], is shown below the solidus line from pure C_{20} to pure C_{22}.

That representation is not compatible with Palatnik and Landau's rule on the adjacent phase domains. This phase β_0 must most probably correspond to the Rotator

phase β-RI (Fmmm) [17,19] and undergo peritectoid decompositions to form the phase α-RII below the solidus line, as in the C_{24}–C_{26} diagram (Figs. 6 and 7).

4. Conclusion

A joint structural and thermodynamic study has enabled us to determine the C_{24}–C_{26} phase diagram. The work has shown that this diagram is more complex than that presented by Mazee [7]. These mixtures, in the same way as the C_{20}–C_{22} [24] and C_{22}–C_{24} [3] systems, do not form a continuous homogeneous solid solution except in the α-RII phase, which appears in the "high temperature" range below the solidus curve and which exists in the two pure *n*-alkanes.

At "low temperature" the two consecutive even-numbered *n*-alkanes are partially miscible, as has been already predicted by Kravchenko [25].

Finally, our study has confirmed the similarity between the phase diagrams of the binary systems composed by two consecutive even-numbered *n*-alkanes from *n*-eicosane to *n*-hexacosane [26,27]. These results enable us to consider a systematic approach to the treatment of the thermodynamic functions of the mixtures of these different binary systems.

The behaviour of *n*-alkane binary mixtures is similar to that of metal alloys, i.e. they are molecular alloys.

References

[1] Z. Achour, J.B. Bourdet, D. Petitjean and M. Dirand, J. Mol. Struct., 354 (1995) 197.
[2] N. Hasnaoui, J. Dellacherie, L. Schuffenecker, M. Dirand and D. Balesdent, J. Chim. Phys., 85(2) (1988) 153.
[3] Z. Achour, P. Barbillon, M. Bouroukba and M. Dirand, Thermochim. Acta, 204 (1992) 187.
[4] Z. Achour, J.B. Bourdet, M. Bouroukba and M. Dirand, J. Chim. Phys., 89 (1992) 707.
[5] A.R. Gerson and S.C. Nyburg. Acta Crystallogr. Sect B: 50 (1994) 252.
[6] W.M. Mazee, Am. Chem. Soc., Meeting Symp. Div. Pet. Chem. (Chicago), 1958, 98.
[7] W.M. Mazee, Erdoel und Kohle, 13(2) (1960) 88.
[8] W.R. Turner, Ind. Eng. Chem. Prod. Res. Develop., 10(3) (1971) 238.
[9] S.P. Srivastava, J. Handoo, K.M. Agrawal and G.S. Joshi, J. Phys. Chem. Solids, 54(6) (1993) 639.
[10] L.S. Palatnik and A.I. Landau, Phase Equilibria in Multicomponent Systems, Holt, Rinhart and Winston, New York, 1964.
[11] I. Denicolo, J. Doucet and A.F. Craievich, J. Chem. Phys., 78(3) (1983) 1465.
[12] J. Doucet and A.J. Dianoux, J. Chem. Phys., 81(11) (1984) 5043.
[13] J. Doucet, I. Denicolo, A.F. Craievich and C. Germain, J. Chem. Phys., 80(4) (1984) 1647.
[14] J. Doucet, I. Denicolo, A. Craievich and A. Collet, J. Chem. Phys., 75(10) (1981) 5125.
[15] R.G. Snyder, A.F. Maroncelli, S.P. Qi and H.L. Strauss, Science, 214(9) (1981) 188.
[16] I. Denicolo, A.F. Craievich and J. Doucet, J. Chem. Phys., 80(12) (1984) 6200.
[17] G. Ungar, J. Phys. Chem., 87 (1983) 689.
[18] S.K. Filatov, E.N. Kotelnikova and E.A. Aleksandrova, Kristallogr., 172 (1985) 35.
[19] G. Ungar and N. Masic, J. Phys. Chem., 89 (1985) 1036.
[20] N. Hasnaoui, J. Dellacherie, L. Schuffenecker and M. Dirand, J. Chim. Phys., 85(6) (1988) 675.
[21] E. Calvet and H. Prat, Microcalorimètrie. Applications Physiochimiques et Biologiques, Masson, Paris, 1956.

[22] D.A. Ditmars, S. Ishihara, S.S. Chang and G. Bernstein, J. Res., 87(2) (1982) 159.
[23] A. Sabour, J.B. Bourdet, M. Bouroukba and M. Dirand, Thermochim. Acta, 249 (1995) 269.
[24] H. Luth and S.G. Nyburg, Mol. Cryst. Liq. Cryst., 27 (1972) 337.
[25] V. Kravchenko, Acta Physicochim URSS, 21 (1946) 335.
[26] Z. Achour, J.B. Bourdet, M. Bouroukba and M. Dirand, J. Chim. Phys., 90 (1993) 325.
[27] P. Barbillon, L. Schuffenecker, J. Dellacherie, D. Balesdent and M. Dirand, J. Chim. Phys., 88 (1991) 91.